Journal of Materials Chemistry A

ROYAL SOCIETY OF CHEMISTRY

PAPER

View Article Online
View Journal | View Issue

Cite this: J. Mater. Chem. A, 2022, 10, 2374

Protagonists and spectators during photocatalytic solar water splitting with $SrTaO_xN_y$ oxynitride†

Craig Lawley, [ab] Zahra Pourmand Tehrani,[ab] Adam H. Clark, [a] Olga V. Safonova, [a] Max Döbeli,[c] Vladimir N. Strocov,[a] Thomas J. Schmidt, [ad] Thomas Lippert,[abe] Maarten Nachtegaal*[a] and Daniele Pergolesi *[a]

Received 15th June 2021
Accepted 21st September 2021

DOI: 10.1039/d1ta05052d

rsc.li/materials-a

Oxynitrides have been shown to be promising visible light water splitting photocatalysts, but rapidly degrade under operating conditions. With a custom designed photoelectrochemical cell, we perform operando grazing incidence X-ray absorption spectroscopy measurements on the oxynitride semiconductor $SrTaO_xN_y$ during photocatalytic solar water splitting. We show that the nature of the A-site (Sr) and its evolution during operation have large impacts on the overall stability and catalytic activity of the material, leading to an enriched BO_2 (Ta(OH)/TaO(OH)) like surface. However, this usually beneficial effect with respect to increased surface hydrophilicity has complications for the efficiency of the photocatalytic process, as the OH and O(OH) intermediates formed are in competition between O_2 generation and NOx species formation in the initial stages of operation. *Operando* characterisation of the evolution of the electronic structure of the photocatalyst proves to be an invaluable tool for the rational design and discovery of new and better performing materials.

Introduction

Independence from the reliance on fossil and nuclear fuels requires the sustainable production of green energy and chemicals. As an alternative, utilisation of solar energy is possible by several means: solar thermal applications,[1] the direct conversion to electricity (photovoltaic),[2] or storage in the form of chemical energy as solar fuels.[3] One promising clean energy carrier and renewable fuel source is hydrogen harvested from photoelectrochemical (PEC) water splitting.[4–6]

PEC water splitting requires the use of semiconductor (SC) photocatalysts that utilise solar light energy to generate electron/hole pairs. After reaching the surface, in contact with water, these charge carriers can be used to dissociate water molecules directly into molecular hydrogen and oxygen.[7] Perovskite oxynitrides are a promising class of SC materials for solar light driven water splitting. These materials have the general formula $ABO_{3-x}N_x$ (where A can be La, Sr, Ba, Ca, *etc.*, and the B site: Ti, Ta, or Nb for example). The substitution of N into the O site of the precursor oxides affect the energy position of the band edges, reducing the band gap down to the visible light energy range.[8] Moreover, in this class of compounds, the photogenerated electrons and holes, both possess enough energy to promote the hydrogen and oxygen evolution reaction, respectively.

The majority of studies to date focus on the characterisation of the photocatalytic properties of these materials in the form of powders,[9–11] since powder development and optimisation is the primary way to device design and engineering. However, with powder samples, probing specific material properties is challenging. For example, the polycrystalline oxynitride powders do not provide well-defined surfaces to allow detailed studies of the solid–liquid interface, where the electrochemical reactions take place. The understanding of the catalytic process at the solid–liquid interface of oxynitride materials is therefore limited, as a result. A way to circumvent this limitation is the growth of thin films. By physical or chemical vapour deposition methods, it is possible to fabricate thin films with well-defined and atomically flat surfaces, therefore representing ideal model systems that allow the investigation of the surface and interface properties.

In this work, we present an *operando* study of the evolution of the photocatalyst semiconductor/water interface during photoelectrochemical solar water splitting using $SrTaO_xN_y$ (STON) thin films. Grazing incidence X-ray absorption spectroscopy (GIXAS) coupled with modulation excitation (ME)-XAS were used to increase the surface sensitivity, whilst probing epitaxially grown STON thin films with a custom designed *operando* reactor cell. This technique and experimental setup allow us to probe, during operation conditions, the changes of the local

[a]Paul Scherrer Institute (PSI), CH-5232 Villigen, Switzerland. E-mail: daniele.pergolesi@psi.ch; maarten.nachtegaal@psi.ch
[b]ETH Zürich, Laboratory of Inorganic Chemistry, CH-8093 Zurich, Switzerland
[c]ETH Zürich, Laboratory of Ion Beam Physics, CH-8093 Zurich, Switzerland
[d]ETH Zürich, Laboratory of Physical Chemistry, CH-8093 Zurich, Switzerland
[e]International Institute for Carbon-Neutral Energy Research (I2CNER), Kyushu University, 744 Motooka, 819-0395 Fukuoka, Japan

† Electronic supplementary information (ESI) available. See DOI: 10.1039/d1ta05052d

chemical and geometric environment surrounding the A- and B-cations of perovskite oxynitrides near and at the solid–liquid interface. Due to the attenuation of X-rays by the aqueous electrolyte, it is not feasible to extend this study to the O and N anions, since the O 1s and N 1s edges are too low in energy (543.1 eV and 409.9 eV, respectively). Therefore, complimentary *ex situ* X-ray photoelectron spectroscopy (XPS) has been included to observe all four elements (Sr, Ta, O, and N) in their initial and final states. STON was chosen as it has been reported to be a promising visible light responsive photocatalyst material.[12] There are also reports that STON is a possible ferroelectric.[13] Various studies have also shown that ferroelectric polling can increase the photocatalytic activity.[14–16] Therefore, STON is a representative material to study several enhancement techniques with the aim to improve and design better performing materials. With this experimental strategy, we are able to show that it is possible to achieve a better understanding of the physicochemical processes occurring at the oxynitride–liquid interface, leading to a degradation of the photocatalytic activity. Our findings can be of great importance for the rational design of stable oxynitride SC's for solar water splitting.

Results and discussion

Photoelectrochemical water splitting

The splitting of water into molecular H_2 and O_2 is an energetically unfavourable reaction. It requires a standard Gibbs free energy change of +237.2 kJ mol^{-1}, which also corresponds to a potential of 1.23 eV per electron. Moreover, for both half reactions of the solar water splitting process to proceed, that is the hydrogen evolution reaction (HER) and oxygen evolution reaction (OER), first the kinetic overpotentials must be overcome. Therefore, a suitable SC material for visible light PEC water splitting should have (a) a band gap in the range of 1.6–2.4 eV to sufficiently utilise the solar spectrum and drive the reactions, and (b) energy position of the band edges appropriately aligned with respect to the HER and OER redox potentials.

As mentioned above, a number of oxynitride perovskite materials possess these characteristics, making them ideal candidates for PEC solar water splitting.[8,9,11,17,18] Thin films of these materials provide excellent model systems to probe the physical and chemical evolution of the surface of the SC, in contact with water. Fig. 1 shows the energy diagram schematic for PEC water splitting using a STON thin film as a light harvesting SC photocatalyst and TiN as the current collector. In Fig. 1a, we see that upon light irradiation with photons with an energy ($h\nu$) > 1.23 eV, the photon is absorbed promoting a photoexcited electron (e^-) from the valence band (VB) to the conduction band (CB). The photoelectrons travel *via* a TiN current collector layer and external circuit where they are involved in the HER using a platinum counter electrode (cathode). The generation of a photoelectron leaves behind a photogenerated electron–hole (h^+) which migrates towards the surface of the SC oxynitride where it is then involved in the OER.

Fig. 1b shows the three-electrode configuration used in this work, where the STON SC photocatalyst is used as a photoanode

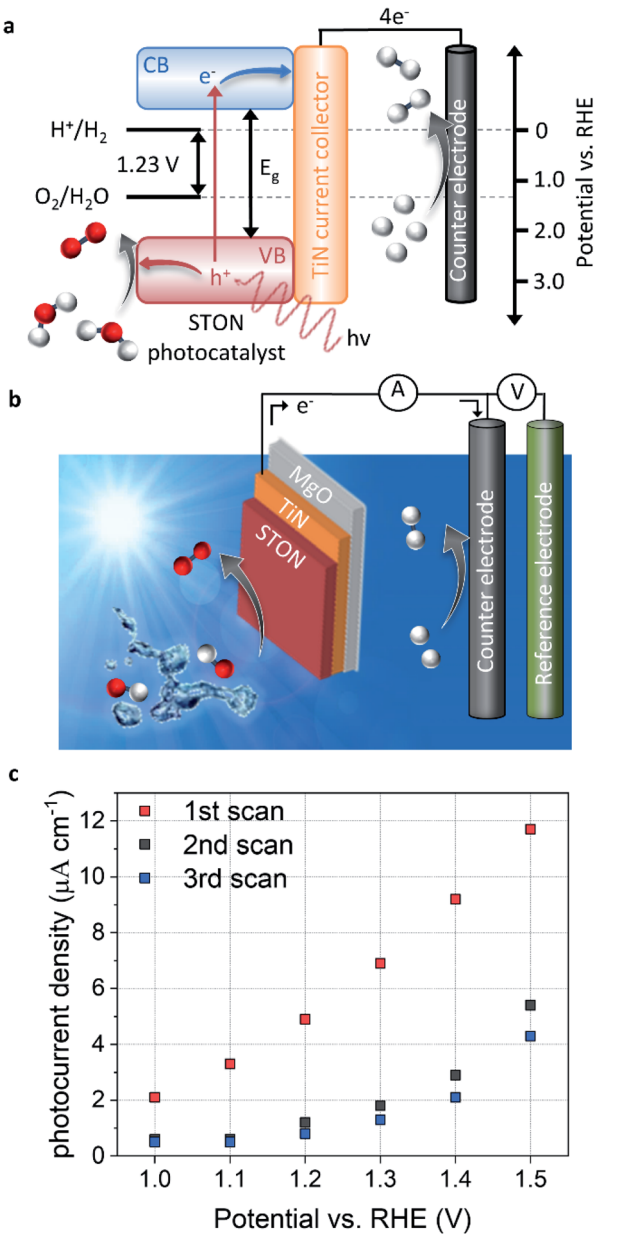

Fig. 1 Photoelectrochemical characterisation (a) experimental schematic of the photoelectrochemical three electrode cell. The working, counter and reference electrodes are the oxynitride thin film, platinum wire and Ag/AgCl respectively, (b) energy diagram for photocatalytic water splitting, (c) photocurrent densities for STON for the first three potentiodynamic measurements, showing initial degradation.

to study the OER, a platinum counter electrode used for the HER half reaction, and a Ag/AgCl reference electrode is used to control the applied potential on the working electrode. The electronic current between the working and counter electrodes is called the photocurrent and the photocurrent is proportional to the amount of molecular H_2 and O_2 produced.

The photocurrent is defined as the current response under light conditions minus the current response under dark conditions. More in-depth experimental details are included in the corresponding methods section. Fig. 1c shows the PEC

performance of the STON oxynitride thins. For sake of clarity, the dark current has been subtracted (ESI Fig. 2†). The initial photocurrent reaches a photocurrent density of *ca.* 12 μA cm^{-1} at 1.5 V *vs.* reversible hydrogen electrode (RHE). This value is in line with previous reports on oxynitride thin films using the bare SC material without surface decoration with co-catalyst, which dramatically facilitate hole extraction. On the one hand, the N content of textured thin films is typically lower than the stoichiometric value that can be obtained with powder samples.[12] This reduces the thin films photo-response to visible light illumination. On the other, the thin films possess atomically flat surfaces compared to the corresponding oxynitride powders. Therefore, the surface area is *ca.* 20 times smaller than it would be in their powder forms. It has been noted that direct comparison of the PEC performances favours the oxynitride powders due to their increased surface area.[19] However, due to the better crystalline quality and the grain morphologies, the oxynitride thin films can show improved charge carrier separation and the subsequent migration to the surface to be consumed in the OER.

However, after successive measurements (potentiodynamic sweeps) the material shows significant degradation in its initial performance. The stabilised photocurrent density shows values *ca.* 40% of its initial value. The sudden and large degradation in performance is a huge hindrance for the application of a material that initially seems quite promising. Some studies have looked at ways of improving the performance and long-term stability of STON[10,20,21] by doping constituent elements and/or decorating the surface with co-catalyst nanoparticles. However, probing the physicochemical evolution of the surface under operation conditions will provide insight into what physical and chemical processes occur at the surface during the OER and therefore, allow a rational design of stable STON.

Oxynitride thin films

The STON thin films were fabricated using a modified pulsed laser deposition technique described in previous works,[22] followed by post annealing in NH_3 for 1 hour. The epitaxial oxynitride STON films were deposited on titanium nitride (TiN) coated magnesium oxide single crystal substrates (001) oriented. Rutherford back scattering (RBS) and elastic recoil detection analysis (ERDA) determined the chemical compositions of the STON thin films as $Sr_{0.94}Ta_{1.06}O_{2.80}N_{0.31}$. The experimental uncertainties for Sr and Ta are ±2% (RBS) and ±7% for O and N (ERDA). The full results have been included in ESI Fig. 1 and ESI Table 1.† The O : N ratio of *ca.* 10 is in line with previous examples of highly ordered oxynitride thin films, since there is a trade-off between overall nitrogen content and crystalline quality,[23] where films with larger N contents tend to be more disordered. Atomic force microscopy and X-ray reflectivity measurements have been included in ESI Fig. 3.†

From Fig. 2 it can be seen that the TiN buffer layer grows (001) epitaxially oriented on the MgO substrate. The (002) reflex of TiN is visible as a shoulder on the left-hand side of the peak of the substrate (see ESI Fig. 4†). Fig. 2 also shows that STON grows epitaxially on the TiN buffer layer[22] with the (*hkl*) reflexes

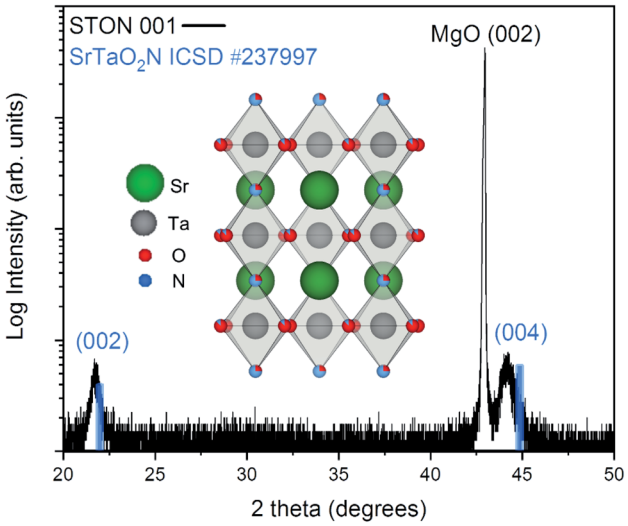

Fig. 2 XRD pattern of the epitaxially grown STON film. The $\theta/2\theta$ scan is shown in black, with the angular position of the (00*l*) reflexes of $SrTaO_2N$ shown in blue for reference. The inset shows the crystal structure of $SrTaO_2N$.

(002) and (004) appearing at 2θ values of *ca.* 21.8° and 44.2°, respectively. The angular position of the (00*l*) reflexes of the perovskite $SrTaO_2N$ have been marked in blue as reference from the Inorganic Crystal Structure Database (ICSD).

There is very good crystallographic matching between the face centered cubic structure of MgO and TiN. The lattice parameters are *ca.* 4.21 and 4.24 Angstrom, respectively. In the pseudo-cubic approximation, the lattice parameter of $SrTaO_2N$ is about 4.03 Angstrom. There is a relatively large lattice mismatch of *ca.* 4.7%, however, the presence of interfacial misfit dislocations, the most common mechanism of stress relaxation in thin films, can easily account for the epitaxial growth of STON on TiN, by releasing part of the strain.

Both the 002 and 004 reflexes of the STON thin film are slightly shifted to lower 2θ values compared to the $SrTaO_2N$ reflexes. This is due to the combined effect of a difference in N content to the stoichiometric reference and the crystalline constrain (lattice mismatch between the substrate and film) induced by the TiN-coated MgO substrate. The perovskite structure of STON remains stable, within a large range of N content. However, the cell parameters can be significantly affected since the N content affects the Ta–O–Ta dihedral bond angle and ultimately, the overall distortion of the cell. To characterise how the OER modifies the physicochemical properties of the surface of our STON films, we first used XPS to compare changes of the oxidation state of all four elements before and after the photoelectrochemical reaction (PECR).

X-ray photoelectron spectroscopy

The XPS spectra for all four elements are shown in Fig. 3, for peak fitting analysis the reader can refer to ESI Fig. 5 and the ESI tables.† Fig. 3a shows the carbon signals that arise due to adventitious carbon, present during the *ex situ* transfer of the samples. After PEC, the intensity of the main peak reduces

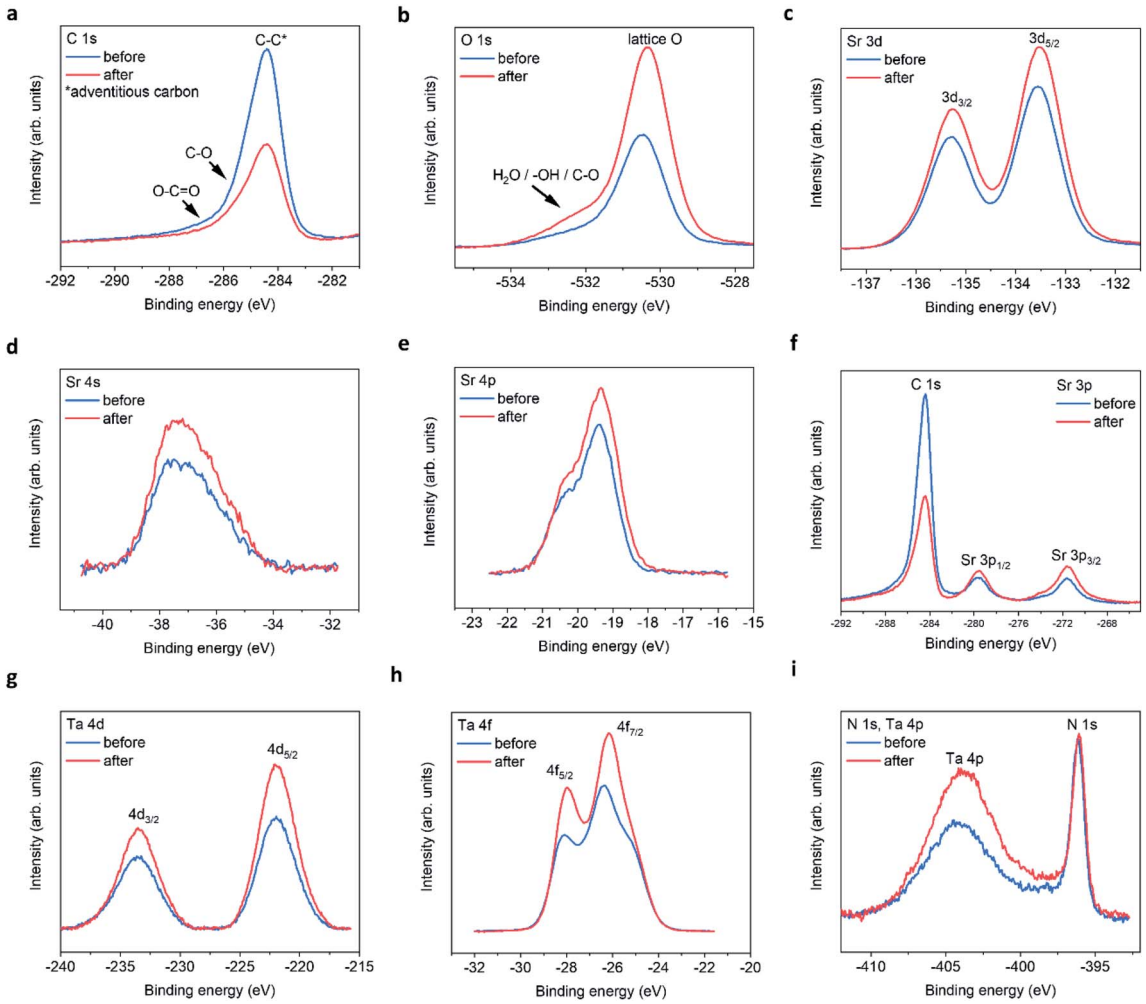

Fig. 3 STON thin film XPS spectra before and after PEC. (a) C 1s, (b) O 1s, (c) Sr 3d, (d) Sr 4s, (e) Sr 4p, (f) Sr 3p, (g) Ta 4d, (h) Ta 4f, (i) N 1s and Ta 4p edges.

suggesting the oxidation/loss of the carbon-based surface contaminates after exposure to the electrolyte and/or X-ray beam. The shoulder features result from C–O and O–C=O like environments. Although, the intensities of the main peak reduce in intensity after PEC, suggesting that the total number of C based species are reduced after PEC, the peak fit suggest that the shoulder C–O contribution increases after PEC, likely due to oxidation during the PEC reaction. With respect to oxygen, after PEC, the O 1s spectra (Fig. 3b) exhibits a large increase in the intensity of the main peak and shoulder feature(s). The shoulder feature is observable on the high-energy side of the asymmetric O 1s lattice peak at *ca.* 531.5–534 eV. It is likely in reality that there exists a number of O based chemical environments (lattice O, SrO, C–O, OH and H_2O). Trying to estimate these environments would produce a high degree of uncertainty in the peak fit models. However, peak fitting suggests a minimum of two chemical environments likely associated with chemisorbed OH and/or H_2O species.

In addition, after PEC the integrated area under of the shoulder increases, suggesting an increase in hydrophilicity of the surface. The increased O content suggests that any lattice vacancies generated at the surface/surface layers are self-healed under OER conditions by oxygen based species.[24]

For the Sr 3d spectra (Fig. 3c), peak fitting suggests that the epitaxial STON thin films as grown exhibit a preferential AO (SrO) termination, also noted for various perovskites using low energy ion scattering (LEIS)[25–29] and XPS.[29–31] Under ambient conditions/aqueous environment, Sr should be covered in OH adsorbates. After deprotonation (slow step) the OER would proceed, leaving vacant oxygen cavity on Sr, assuming the traditional 4-step mechanism for the OER.[32] However, SrO is partially soluble in water to form ionic Sr^{2+} and $2OH^-$. Therefore, dissolution and leaching of Sr^{2+} into the electrolyte would be expected.[33] Especially, in an alkaline medium such as NaOH/H_2O with a pH of 13.

After PEC, the peak fitting suggests a large decrease in the SrO content at the surface and an overall increase in peak area and intensity for the remaining Sr XPS spectra (Fig. 3c–f). It has previously been shown, that an increase in XPS peak intensity can result from Sr segregation/accumulation[34,35] as well as, with increased doping concentrations.[36] Peak intensity/area increases are also observed due to Sr particle/Sr surface

species formation.[34,35] Therefore, the increase in Sr signal in this work is likely due to the loss of SrO and the apparent enrichment of the Sr lattice contribution.

Fig. 3g–i, include the Ta 4d, Ta 4f, and Ta 4p edges respectively. From peak fitting the Ta 4d spectra suggests one binding environment, which is the lattice Ta contribution. After the PECR, this intensity and area of the Ta 4d peak increases as seen for the lattice Sr contributions. This suggests that after the loss of SrO the underlying lattice Ta appears enriched by XPS. The Ta 4f spectra (Fig. 3h) exhibits two peaks due to the Ta $4f_{5/2}$ and $4f_{7/2}$ contributions. The peak fitting analysis suggests that there are two Ta binding environments for both the 5/2 and 7/2 peaks corresponding to TaO_x and TaO_xN_y like environments (ESI Fig. 5†) which, after the PECR, the peak contributions of TaO_xN_y decrease and those of TaO_x increase. Again, like the O 1s spectra, suggesting a slight loss of nitrogen and an increase in the overall oxygen content at the surface/surface layers of the thin film. The energy positions of the peaks suggest a slight reductive shift by *ca.* +0.15 eV. However, the Ta 4d spectra in Fig. 3d show an increase in the FWHM and peak intensities, but no shift in energy position or peak separation. The shift in the Ta 4f spectra may then also be related to the changing O/N, resulting in disorder and differences in the charge transfer between the Ta 4f final states and the O 2p/N 2p orbitals. This then shifts the mid gap f band higher towards the CB or above,[37] leaving the 4d core states unchanged. The increase in intensity observed could be a result of apparent lattice Ta enrichment due to the O/N vacancy generation exposing the subsurface B sites.[27] It could also be a result of SrO leaching, also exposing the subsurface Ta on average. Since Sr is more soluble than Ta and, it has been shown that Ta is passive in alkaline electrolytes with concentrations 2.5× stronger than used in this work.[38]

The electronic configuration of Ta^0 is [Xe] $4f^{14}5d^36s^2$ and that for Ta^{5+} should then consist of [Xe] $4f^{14+}$. This may then explain, the changes in charge transfer and hybridisation between the Ta 4f and O/N 2p atomic orbitals as observed in this work and suggested by the peak fitting analysis. This is also interesting as the f orbitals are typically ignored when considering the density of states (DOS) using density functional theory (DFT) calculations for materials due to the complexity, time and cost involved in the computation of the f states.

The Ta $4p_{3/2}$ is observed as a broad peak at *ca.* 404–405 eV (Fig. 3e). However, the Ta $4p_{3/2}$ spectrum overlaps with the N 1s signal in the energy region at *ca.* 402–408 eV which contains the N 1s information regarding interstitial and/or chemisorbed NO, NO_2, NO_3 and N_2, making the peak analysis difficult. The N 1s Ta–N lattice signal can be seen as a sharp peak at *ca.* 396.1 eV. After the PECR, the broad peak in the region, which contains the convoluted N 1s and Ta $4p_{3/2}$ signals increases significantly suggesting an increase in the number of electronically decoupled N states. As well as, the apparent lattice Ta enrichment as seen previously.

At *ca.* 407.5 eV there is a small but obvious increase in intensity belonging to a different Ta/N binding state, which is likely a contribution due to chemisorbed NO_3 according to literature reports (ESI Table 5†). It is therefore assumed that NO and NO_2 would contribute to the overall increased intensity/peak area observed, where the O(OH) OER intermediate formed during the reaction likely oxidise the NO_x species in competition with O_2 evolution. This would reduce the overall efficiency of the material, and chemisorbed NO_x species would occupy possible active sites. This, in conjunction with the surface reconstruction after the loss of SrO and the changing N/O content, could explain the large degradation in initial photocurrent observed. Likely hampered by side reactions and charge recombination.

Clearer evidence of NO_x formation for the oxynitride $LaTiO_xN_y$ where Ta does not convolute the N 1s signal can be seen by XPS (ESI Fig. 5†). We would like to focus our discussion on the PEC nitrogen evolution reactions at the surface of the oxynitride SC, since the literature on this topic is scarce. Although, this process seems to have important consequences on the oxygen and hydrogen evolution half reactions.

Photocatalytic nitrate formation on Ti dioxide surfaces irradiated by UV or sunlight irradiation under atmospheric N_2 and O_2 has been discussed by Yuan *et al.*[39] Where the photogenerated holes on the Ti SC surface catalyse the intermediary NO_x species according to the following reactions given by eqn (1) and (2):

$$N_2 + O_2 \rightarrow 2NO \quad (1)$$

$$N_2 + 2H_2O + 4h^+ \rightarrow 4H^+ + 2NO \quad (2)$$

Dai *et al.*[40] recently looked at the nitrogen oxidation reaction (NOR) catalysed by Fe/Co spinel oxides in alkaline electrolyte. Where they show that adsorbed N_2 is oxidised to intermediate NO_x species by the adsorbed OH and the OER intermediate O(OOH) according to eqn (3) and (4):

$$N_2 + 2OH^- \rightarrow N^* + NO + H_2O + 2e^- \quad (3)$$

$$N^* + 2OH^- \rightarrow NO + H_2O + 2e^- \quad (4)$$

where the intermediate NO_x species are oxidised given by eqn (5) and (6):

$$NO + 2OH^- \rightarrow NO_2 + H_2O + 2e^- \quad (5)$$

$$NO_2 + 2OH^- \rightarrow NO_3^- + H_2O + e^- \quad (6)$$

With the aid of theoretical calculations, the authors note that Co shows increased hybridisation with the O 2p states, which aids in the stabilisation of OH^- adsorption. This superficial CoO(OH) enriched surface layer has a beneficial effect on the OER for the oxides.[40,41] However, in the presence of surface nitrogen based species, the stabilised CoO(OH) contribute to both the NOR and OER.[40]

Kato and Kudo[42] looked at numerous tantalate oxide photocatalysts, and the authors observed nitrate reduction under UV irradiation in an aqueous environment. Where nitrate forms intermediate nitrite, dinitrogen and ammonia, even in the absence of a co-catalyst or reducing agents. The authors proposed the following mechanisms shown in eqn (7)–(10):

$$NO_3^- + 2H^+ + 2e_{CB}^- \rightarrow NO_2^- + H_2O \quad (7)$$

$$NO_2^- + 7H^+ + 6e_{CB}^- \rightarrow NH_3 + 2H_2O \quad (8)$$

$$2NO_3^- \rightarrow 2NO_2^- + O_2 \quad (9)$$

$$2NH_3 + 6h_{VB}^+ \rightarrow N_2 + 6H^+ \quad (10)$$

where the photogenerated electrons in the CB reduce the nitrate and nitride species (eqn (7) and (8)). Alternatively, the nitrate species can undergo photochemical decomposition (eqn (9)). The photogenerated holes in the VB can then oxidise ammonia to form dinitrogen (eqn (10)), which can form NO_x species according to eqn (1)–(4).

Wei *et al.*[43] recently reported increased photocatalytic activity for nitride reduction on Ni_2P modified tantalum nitride and tantalum oxynitride (Ta_3N_5 and TaON, respectively). Where the photogenerated holes in the VB of the two materials are involved in the water oxidation reaction (eqn (12)) and, the photogenerated electrons in the CB transfer to the Ni_2P states where they are involved in the photocatalytic reduction of NO_3^-. For a detailed overview on the role of N in electrocatalysis, the readers are directed to the work by Rosca *et al.*[44]

The photocurrent is proportional to stoichiometric 2 : 1 H_2/O_2 generation, according to the two half reactions of the water splitting process on a SC photocatalyst (eqn (11) and (12)).

$$4H^+ + 4e_{CB}^- \rightarrow 2H_2 \quad (11)$$

$$2H_2O \rightarrow 4h_{VB}^+ + O_2 + 4H^+ \quad (12)$$

As the potential increases, the forward reactions for O_2 generation dominate since the nitrogen content at the surface is limited, compared to the high OH^- content in the alkaline electrolyte. Once the nitrogen species desorbs from the surface, the OER could proceed on the now vacant active site and/or the adsorbed intermediates would no longer contribute to N_2/NO_x formation in competition. As shown by the increase in photocurrent density as seen in Fig. 1c and 6b. However, the above-mentioned changes for STON result in a surface reconstruction during the initial stages of operation, reducing its long-term performance.

As previously discussed, the CB of STON is primarily comprised of Ta 5d states (no f state information). Considering the changes in the disorder, especially the local disorder surrounding the Ta cations, this would result in generation of defect Ta states at/near to the CB minimum or, even mid bandgap defect states. These defect states would trap the photogenerated electrons, leading not only to charge recombination, as previously discussed but also, contribute to the reduction of the generated nitrate species (eqn (7) and (8)) as suggested by the works by Kato and Kudo (2002),[42] Wei *et al.* (2020)[43] and the XPS analysis in this work.

The CB minimum and VB maximum of STON incorporate not only the redox potentials of the OER and HER, but also those for NO_3^-/NH_4^+ (0.88 V), NO_3^-/HNO_2 (0.94 V) and NO_3^-/N_2 (1.24 V) at pH = 0, *vs.* NHE.[43] This implies that all photogenerated electrons consumed in these competing reactions would no longer contribute to the HER at the Pt counter electrode (Fig. 1a), reducing the potential magnitude of the photocurrent density. The photogenerated holes that do not recombine would then primarily contribute to water oxidation (eqn (12)).

The surface nitrogen that remains chemisorbed in the form of molecular N_2/NO_x would likely, (a) occupy possible O_2 generation sites, effectively blocking the site until it desorbs or, (b) reduce or oxidise to form additional chemisorbed N_2/NO_x species as suggested by XPS. The apparent mechanism is likely then associated with one or more of the previously discussed eqn (1)–(10). Since the electron density surrounding Ta is conserved, the nitrogen vacancies generated are then likely healed by the OER intermediate adsorbates.[24] The changing stoichiometry, tensile strain and changes in the charges of the surface layer result in a surface reconstruction that would affect the surface binding energies of the intermediate products produced during OER conditions (*OH, *O, *OOH). The intermediates that adsorb too weakly or too strongly will reduce the overall kinetics and, increase the overpotential of the OER.[24,45]

To conclude, OER and HER remain the dominant reactions, however the initial reconstruction and the following competitive reactions, limit the overall efficiency of STON compared to its initial performance. The XPS analysis of the initial and final state of the STON photocatalyst suggest that STON suffers from a surface degradation and reconstruction, which lead to a dramatic decrease in photocurrent (Fig. 1c). This process involves (a) loss of surface terminated SrO, (b) enrichment of lattice Sr and Ta, (c) change in hybridisation/charge transfer between the N and O 2p, (d) oxidation of NO_x species in competition with O_2 generation, and (e) increase in hydrophilicity (oxygen content at surface).

Next, we explore the effect of several external stimuli (applied potential and light) on the surface of the oxynitride SC under oxygen evolution reaction conditions by *operando* XAS in liquid phase.

Operando reactor cell

The *operando* XAS measurements were performed in a custom-built reactor cell designed and fabricated at the Paul Scherrer Institute for the specific purpose of *operando* GIXAS in aqueous electrolytes for thin films. The cell design is schematically depicted in Fig. 4.

The cell is made of polyether ether ketone (PEEK), a thermoplastic with high mechanical and chemical stability, allowing the use of most common acidic/alkali based aqueous electrolytes. The X-ray beam illuminates the surface of the sample at grazing angle and the fluorescent signal is detected as a cone along the surface normal, as shown in Fig. 4a. The surface sensitivity that can be achieved in grazing angle geometries considering the incident energy of the X-rays is *ca.* 3 nm.[46] The cell is designed to hold thin films grown onto standard substrate sizes. Typically, 10 × 5 mm or 10 × 10 mm with a substrate thickness of 0.5–1.0 mm. The window material used is an optically clear Mylar foil (t = 0.19 mm), which allows the transmission of visible light onto the sample whilst also

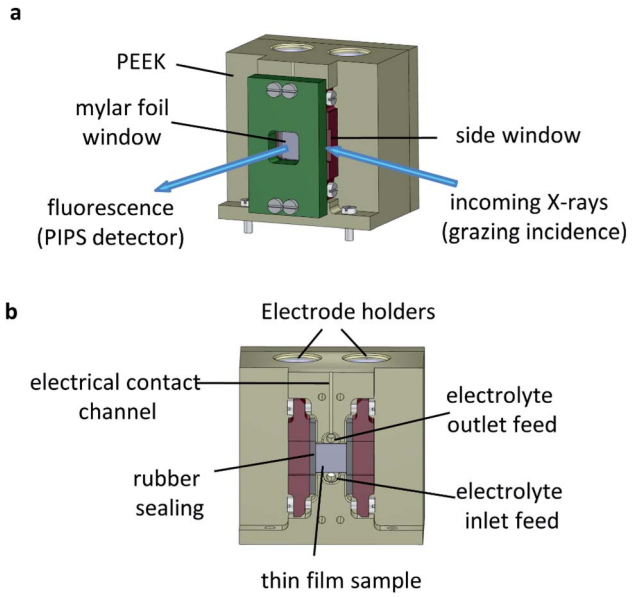

Fig. 4 *Operando* reactor cell for surface sensitive GIXAS measurements. (a) Trimetric view of the cell and GIXAS geometry used during measurements, where the grazing incident X-rays enter through a Mylar foil covered side window (PIPS denotes a passivated implanted planar silicon detector), (b) cross sectional internal view.

allowing >90% X-ray transmission at the energy ranges used in this work (ESI Fig. 6†). The use of Mylar foil as a window provides flexibility in enabling visible light to shine onto the sample whilst detecting the fluorescence signal, as well as allowing grazing incidence angles of <1° onto the sample surface in an aqueous environment. Synthetic rubber pieces clamped into position seal the Mylar foil window to prevent leaks (Fig. 4b). On the backside (ESI Fig. 7†) are two threaded openings, allowing the use of an external electrolyte reservoir as well as connecting a peristaltic pump or a syringe pump system to circulate the electrolyte as required. Alternatively, the cell can use an internal electrolyte reservoir situated behind the sample. The cells' internal reservoir can house both the counter and reference electrodes.

Tantalum L_3 edge XANES

Fig. 5a shows the XANES spectra recorded *ex situ* at the Ta L_3 edge (E_0 = 9881 eV) for $BaTaO_2N$ (BTON), STON, and $KTaO_3$ powder samples. These measurements are used as reference to understand the corresponding GIXAS measurements performed during OER using the STON thin films, as shown in Fig. 5b. We use $KTaO_3$ as a reference for this work since the parent oxide of STON, which would be $Sr_2Ta_2O_7$, possesses a different crystal structure, therefore, the electronic structure would differ significantly. $KTaO_3$ has a cubic crystal structure like $SrTaO_2N$ and $BaTaO_2N$. Moreover, in all three cases Ta exists in the 5+ oxidation state, therefore allowing a sensible comparison of their electronic structures (Fig. 5a). We can see that, compared to $KTaO_3$, for the oxynitride powders there is a shift of the edge position (E_0) to lower energies by *ca.* 0.5 eV ± 0.1. This shift of the absorption edge is not due to the reduction of Ta but rather due to the downward shifting of the CB minimum of STON and BTON compared to $KTaO_3$. Since, the CB is comprised of Ta 5d orbitals for all three materials.[47] The substitution of nitrogen into the oxygen sites affects the Ta–O/N–Ta dihedral bond angle and the overall electronegativity of the anions. Both these effects can explain the downward shift in energy of the CBM.[48,49]

The increase in intensities for the XANES spectra most likely result from the nitrogen substitution. In the cubic perovskite oxide $KTaO_3$, the Ta–O–Ta angle is 180°. In the orthorhombic oxynitride perovskites, the dihedral bond angle is distorted and its value depends on the total N content and the size of the A cation. Therefore, with the lowering of symmetry and increased p–d orbital mixing, the 2p–5d transition will be more favourable and reflected in the relative intensities of the peaks.

Fig. 5b shows the *operando* XANES measurements performed on STON thin films during the chronoamperometry measurements (measuring the photocurrent at a fixed applied potential over time). We can see that for all applied potentials, there is no significant change in the spectral shape or in the edge position, indicating no change in formal oxidation state. When inspecting the magnified inset, there are small shifts in the edge positions to higher energies when moving from 1.1 to 1.3 and 1.3 to 1.5 V *vs.* RHE, corresponding to *ca.* 0.05 and 0.1 eV respectively.

Baring in mind the experimental uncertainties with respect to the composition provided by RBS and ERDA ($Sr_{0.94}Ta_{1.06}O_{2.80}N_{0.31}$), Ta^{4+} defect centers should exist which are oxidised to Ta^{5+} during the OER. However, it has previously been shown that for various compounds which all contain formally Ta^{5+} species, the edge position can vary by *ca.* 1.4 eV (ref. 50) due to the variation of the electronic structure and the relative position of the Ta 5d states. Therefore, the small shifts seen in edge position for Ta are unlikely to be oxidation of Ta at the surface. Even though oxidation states are often valid interpretations due to the correlation between formal oxidation state and edge position,[51–53] the changes shown here are first, within error and second, any small change is likely due to the slight loss of lattice nitrogen and/or the possible formation of NO_x species at the surface of the STON thin film as suggested by the XPS analysis in this work. As previously discussed, upon partial N loss in the surface layer, it will also result in a local loss of hybridisation between the Ta 5d and the N 2p states at the VB maximum (Fig. 5c). As a result, a more 'oxide-like' electronic structure forms at the surface as the potential is increased.

It is reasonable to assume that Ta will tend to fulfil its full coordination sphere upon loss of N by replacing with O under OER conditions.[24] This would also explain why there is no significant change in the spectral shape for Ta. There is instead, a slight shift to higher energy of the absorption edge. However, the replacement of N^{3-} with O^{2-} should see a reductive shift to lower energy for Ta. This again suggests that the charge around Ta is stabilised, like for Ti in $LaTiO_xN_y$,[46] but due to slight changing O/N concentrations at the surface, the Ta octahedra undergo a slight disorder. Since the CBM is comprised of delocalised Ta 5d states in STON,[54] the resulting changes in the

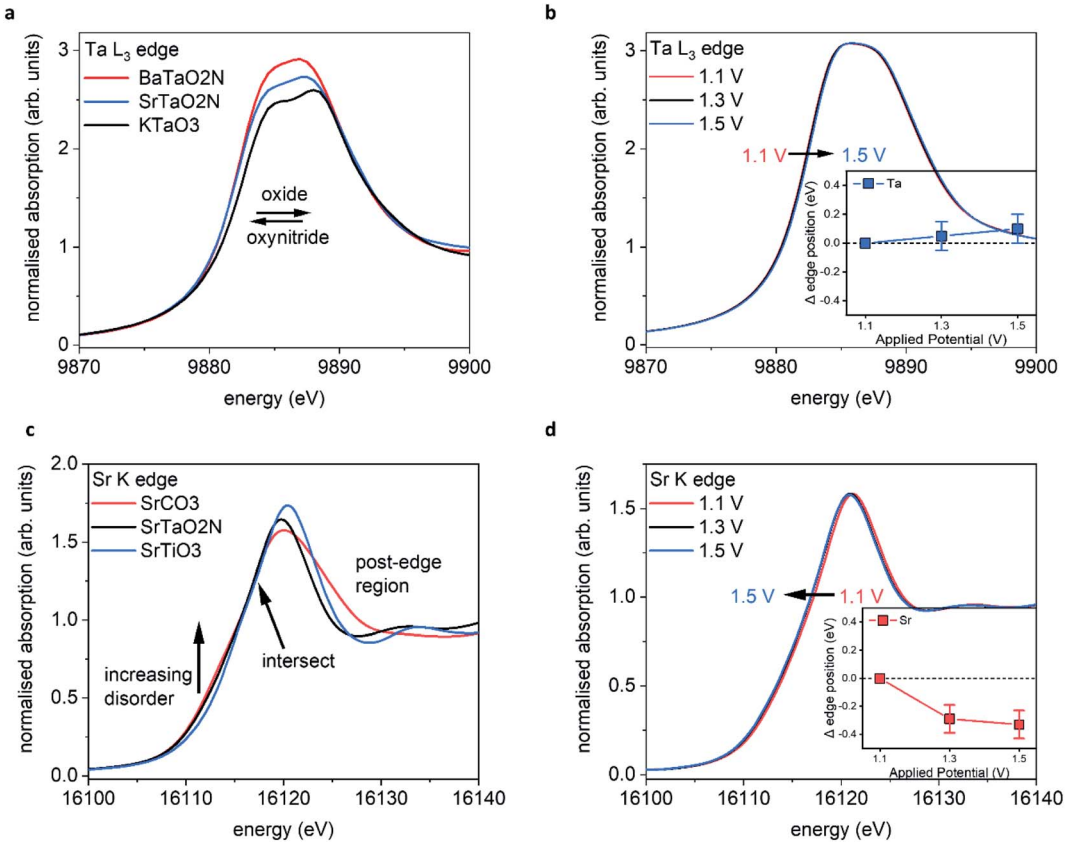

Fig. 5 *Operando* GIXAS at the STON–liquid interface (a) reference spectra for Ta^{5+} oxide and oxynitride powders, (b) *operando* Ta measurements for STON thin film, (c) reference spectra for Sr^{2+} containing powders, (d) *operando* Sr measurements. The *operando* characterisations were performed during the chronoamperometry (1 hour) measurements, with stepped applied potential. The error bars included in the magnified inset correspond to ±0.1 eV.

O/N–Ta–O/N dihedral bond angle and degree of hybridisation, affect the conduction band minimum position.[49]

Strontium K edge XANES

Fig. 5c shows the XANES spectra measured at the Sr K edge (E_0 = 16 105 eV) for Sr containing oxide ($SrTiO_3$), carbonate ($SrCO_3$) and oxynitride (STON) powders. Small changes in the post edge region and in the intensities of the main peak (16 120–16 140 eV) can be observed and are due to the differences in coordination environment surrounding the Sr cations.[55] There are also changes of intensity of a broad shoulder in the pre-edge region at *ca.* 16 108–16 115 eV. Pre edge features relate to changes in the local geometry and degree of disorder surrounding the absorbing element of interest. Therefore, as one moves away from a perfect octahedral environment the pre-edge intensities increase[56] and this is observed from the perfect octahedral environment surrounding Sr in $SrTiO_3$, to the increasingly disordered octahedra in $SrTaO_2N$ and $SrCO_3$, respectively.

Fig. 5d shows the *operando* XANES measurements performed on the STON films during the chronoamperometry measurements as described previously. Unlike for the Ta B site, here we observe a more significant shift in the edge position due to an increase of electron density on Sr^{2+}, with increasing the applied potential from 1.1 to 1.3 V *vs.* RHE. Increasing the potential further from 1.3 V to 1.5 V does not show any further significant modification of either the local coordination or electronic structures around the Sr cations. The observed shift in edge position with potential is not constant, unlike observed for Ta.

Many of these oxides and oxynitride perovskites tend to typically exhibit AO (SrO) surface terminations[25,27,57] rather than BO_2 (TaO_2). As previously discussed, a Sr/SrO_x surface initially covered by oxygen adsorbates, would then initially contribute to overall O_2 generation.[47] As the potential increases to 1.3 V, the Sr starts to reduce (Fig. 5d) likely associated with the decoupling of the OER intermediates leaving the adsorption site on Sr vacant[47] before further adsorption.

However, the degradation in the initial performance of STON and the XPS and XAS results, suggests these changes on Sr are permanent and detrimental. When changing the applied potential from 1.3 to 1.5 V, we see no significant change, except an overall further reductive shift albeit, at a reduced magnitude (Fig. 5d inset) within error. This observation could be explained by the earlier discussion regarding the deprotonation of Sr as the overpotential determining step (ODS). As the potential increases the majority of the Sr species reduce, followed by Sr/SrO/SrOH leaching. This disorder would also lead to defect Ta 5d states near the CBM which will then trap electrons,[58] leading to charge-recombination.[59] This, in conjunction with changes

seen for Sr and the generation of N species in competition with O_2 generation, can explain why there is unusually large degradation in the initial photoelectrochemical performance of STON before the material stabilises.

Modulation excitation X-ray absorption spectroscopy

In a different and complementary experimental strategy, we performed modulation excitation XAS (ME-XAS) to monitor the real time effects of the chemical modification of the surface using light as the external stimulus. The description of the experiment can be seen in Fig. 6a, where the thin film sample is stimulated by periodic modulation of light (chopped illumination) whilst time resolved XAS measurements are performed and data collected simultaneously during operation conditions at different, fixed potentials. Spectral changes induced by external stimuli (light in this case) are often small and/or prone to overshadowing by noise and background signals due to the experimental set-up.[60] One can improve the signal-to-noise ratio by averaging data sets over several modulation periods. Furthermore, improvements in signal-to-noise ratio can be achieved through analysis of ME-XAS with phase sensitive detection (PSD).[61–64] PSD converts time-resolved XAS data into a set of phase (φ^{PSD}) resolved data akin to a digital lock-in amplifier, enhancing the sensitivity of the ME-XAS experiment to spectral responses that match the frequency of the chopped

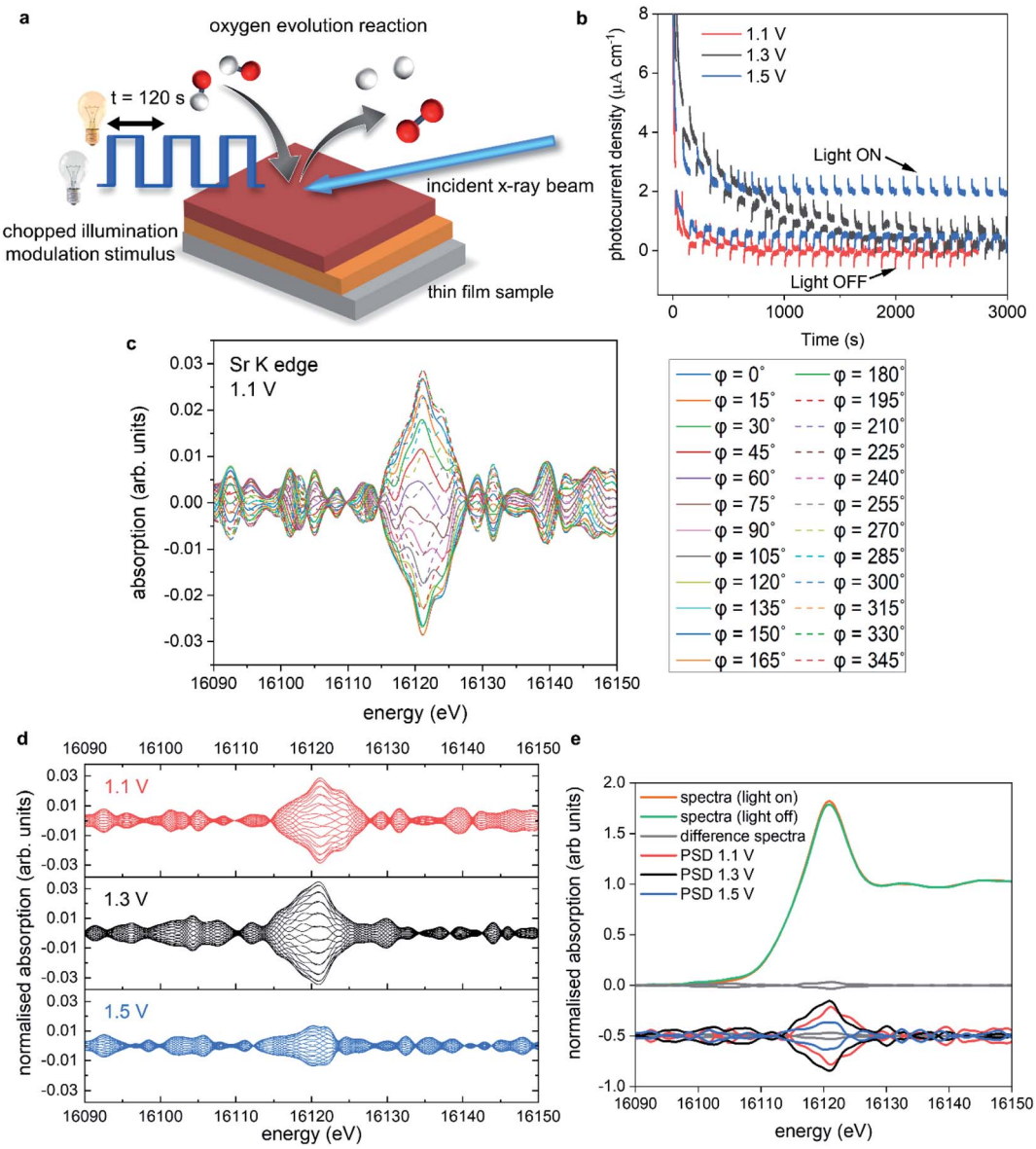

Fig. 6 *Operando* ME-XAS at the STON–liquid interface. (a) Schematic of the experiment, (b) chronoamperometry measurements performed at 1.1 V, 1.3 V and 1.5 V *vs.* RHE, (c) phase resolved spectra ($\varphi^{PSD} = 0–345°$) obtained from the modulation experiment measured at 1.1 V at the Sr K edge, (d) phase resolved spectra for Sr K edge measured at 1.1 V, 1.3 V and 1.5 V *vs.* RHE shown in red, black and blue, respectively, (e) average of spectra recorded under illumination and under dark conditions, with the difference and PSD spectra at each potential.

light stimulus. More information on the PSD approach is included in the ESI Discussion.†

Fig. 6b shows the chronoamperometry measurements at 1.1, 1.3, and 1.5 V *vs.* RHE where the incident light was modulated with 120 second periods (60 seconds on, 60 seconds off). Fig. 6b has been adapted for sake of clarity, where the photocurrent spikes (labelled light ON/OFF), are minimised. At 1.1 V, the photocurrent response is limited, but as the potential is increased further the photocurrent response also increases, as expected. However, at 1.3 V there is a large increase in the dark current response compared to 1.1 V. This increase degrades over time, before minimising after *ca.* 3000 s. When the potential is stepped to 1.5 V, there is an initial increase in the dark current response, which stabilises *ca.* 1/3 faster than at 1.3 V. There is also an overall increase in the stabilised dark current response compared to 1.1 and 1.3 V. These increases in the dark current at 1.3 V also coincide with the changes seen in the *operando* XAS data measured at 1.3 V, with the increase of electron density on Sr, resulting in increased overpotentials.

Fig. 6c shows, as an example, the PSD data analysis of data acquired at the Sr K edge for STON measured at 1.1 V. The benefit of PSD is the significantly enhanced signal-to-noise ratios, as it contains primarily only the signals from the changes due to the external light stimulus,[65,66] while spurious effects from inactive species, spectators and noise are filtered out.

Fig. 6d includes the phase resolved spectra for Sr measured at 1.1, 1.3, and 1.5 V in red, black and blue, respectively. Not only can we see that there are small changes due to stimulus with light, but there is also a potential dependence. The spectra collected at 1.5 V show decreased sensitivity (smaller differences) due to the modulated light stimulus compared to 1.1 and 1.3 V. Fig. 6e shows an example of averaged spectra collected under illumination and dark conditions at one potential, along with the difference of the two plots shown as a solid grey line and the PSD spectra shown below.

Upon irradiation with light, photons with sufficient energy are absorbed; generating electrons and electron–hole pair charge carriers. The charge carriers are subsequently consumed in the water splitting process or recombine. The promotion of electrons from the valence band to the conduction band will induce small changes in the overall electronic system. This is reflected by the change in intensity of the Sr K-edge main peak under illumination (Fig. 6e).

We saw for the XANES (Fig. 5d) that when the Sr species reduce, there is a gain of electron density surrounding Sr with applied potential. The electronic configuration for Sr should reflect [Kr] $5s^2$ and that for oxidised Sr^{2+} represented by [Kr]. Therefore, as Sr reduces with applied potential, one would expect the lower lying energy 5s orbitals to be partially filled compared to the 4d states, according to Hund's rule. Typically, the intensity, especially in the case of L edges, is assumed to be related to holes in the d-band. Therefore, an oxidised species with electron–holes in the d-band would typically exhibit larger intensity of that of a more reduced species with a filled d band.[67] The Sr K edge transition includes dipole s to p transitions like the L edges previously mentioned, however, it also includes quadrupole transitions s > d and p > f, complicating the interpretation further. Especially, as these quadrupole transitions should be forbidden due to selection rules. However, due to disorder and p–d orbital mixing, the forbidden s > d transitions are observable in the K edge spectra. According to p-DOS, the CB for STON is comprised of primarily Ta d states, but also Sr d states and with increasing energy, the Sr p and s states.[54]

This can be reflected visually in Fig. 5d with the pre-edge features of various Sr containing species with, the local coordination surrounding the absorbing Sr showing signs of disorder from the perfect octahedral. With increasing degrees of disorder and orbital mixing, the intensity of the pre-edge features increases, as the usually forbidden s > d transitions are now allowed. Therefore, the main peak intensity may not be solely related to oxidation state and holes in the d band, like for the L edges, but also to the effect of the Sr s and p states and, the local coordination surrounding Sr. As previously mentioned, due to the highly crystalline nature of the epitaxial films, diffraction renders the EXAFS data unreliable to investigate any changes in the local coordination environment of Sr. Future work will look at ways to circumvent this limitation.

As electron density on Sr increases, the reduced intensity of the PSD data at 1.5 V (Fig. 6d) may then be related to (a) reduced probability for an electron to promote to the Sr states in the CB, as they are now partially occupied and/or (b) increased recombination of electron–hole pairs due to the surface reconstruction and the proceeding of the forwards reaction of the OER.

The suggested changes to the surface stoichiometry would result in a surface reconstruction that affects the binding energies of the intermediate products (*OH, *O, *OOH) produced during OER conditions. The intermediates that adsorb too weakly or too strongly will reduce the overall kinetics and, increase the overpotential of the OER.[24,45] At 1.5 V, the applied potential overcomes the increased overpotentials, reflected in the increased photocurrent response.

Both the A (Sr) and B (Ta) are both described as active sites for the OER mechanism to proceed on.[47] With Sr covered in OH adsorbates contributing to O_2 generation. Deprotonation was shown to be the ODS for STON,[47] Therefore, upon deprotonation, most Sr species would exist as SrO which, as previously discussed, is partially soluble in the electrolyte. However, unlike Sr, the Ta PSD signals never increase above the level of noise (ESI Fig. 8†). This suggests either two things: (1) Ta is not responsive to the light and not involved in the photo absorption process, a hypothesis which would contradict available literature[12,47,68] or, (2) the kinetics for Ta are faster than those for Sr[47] therefore Ta evolves O_2 at faster rates.

Conclusion

In this work, we employed *operando* grazing incidence and modulated excitation X-ray absorption spectroscopy to study the effect of several stimuli on STON oxynitride thin films during photoelectrochemical water splitting. A comparison with *ex situ* XPS of the samples in their initial and final states is also included. The XPS analysis suggests (a) partial dissolution of SrO_x into the alkaline electrolyte, (b) an increase in electron

density on Sr, (c) lattice Sr and Ta enrichment at the surface, (d) changes in hybridisation with the N 2p and O 2p states. (e) Increase in surface hydrophilicity, evidenced by the increased adsorbed OH/O(OH)/H_2O content, (f) slight loss of N from the structure where N remains chemisorbed as N_2/NO_x species.

Surface reconstruction under OER conditions has previously been discussed for Sr and Co containing perovskite oxide catalysts[41,69–71] where, the OER proceeds under applied potential together with the lattice-oxygen evolution reaction.[41,72] This has been shown to have a beneficial effect with respect to the OER due to the formation of an enriched BOH/BO(OH) surface, increased hydrophilicity and an increase in catalytic activity.[41,73] For the oxynitride STON, we also observe surface enrichment of the B cation (Ta) and increased hydrophilicity. However, contrary to oxides, this superficial BOH/BO(OH) enriched surface layer may have complications for the oxynitrides. Since, the N 1s XPS analysis of LTON and STON oxynitride thin films before and after the PECR, evidence N_2/NO_x chemisorbed species. As discussed previously, likely formed in competitive reactions from the surface lattice N and the OER intermediates.

Operando GIXAS determined that the surface reconstruction occurs when the applied potential increases above 1.3 V *vs.* RHE. ME-XAS-PSD measurements with modulated light as an external stimulus. It was previously shown for $LaTiO_xN_y$ that light and the electrolyte do not contribute to the degradation of the material.[46] However, we observe small changes in the light response for Sr, with respect to its electronic structure and its evolution as a function of applied potential. Here we show that the nature of the A cation and the evolution of its electronic and geometric environment at the solid/liquid interface has large impacts on the overall stability and catalytic activity of the material during operation conditions.

We also note that nitrogen determines the bulk electronic structure of oxynitrides and in turn, the light absorption properties of the photocatalysts. However, at the surface, the nitrogen species take on a more apparent antagonistic role, competing with the OER. To improve the performance of semiconductor photocatalysts, it is important to understand on a fundamental level what is occurring at the photocatalyst surface during operation.

This study presents the first *operando* surface sensitive characterisation of the solid–liquid interface during the visible light driven oxygen evolution reaction. An important advance, for future work to explore in *operando*, the effect of applied potential and the synergistic effects first row transition metal-based co-catalysts have on the performance and stability of the oxynitride photocatalyst templates, where it has been shown that passivation layers and co-catalysts can prevent/minimise the detrimental surface reconstruction. Future experiments involve the screening of co-catalysts (material, deposition method, time, potential *etc.*) with respect to enhanced performance and stability. With the optimised SC and co-catalyst pairing, the ferroelectric polling enhancement method previously reported can be combined with comparing the 001, 011 and 111 (*hkl*) orientated STON films. The *operando* studies are not limited to the visible-light responsive oxynitrides thin film photocatalysts. *Operando* surface sensitive characterisations and comparisons can also be made with thin films representative UV-only responsive, wide band gap oxides.

Methods

Thin film deposition

Three sets of films used in this work were grown using pulsed laser deposition (PLD). A KrF excimer laser (Lambda Physik LPX 300, 30 ns pulse width, $\lambda = 248$ nm) was used to ablate a target of $Sr_2Ta_2O_7$ fabricated in our laboratory. The target to substrate distance was set at 5 cm. The laser was focused on a spot of 1.1 mm^2 with a laser fluence of *ca.* 3 J cm^{-2} and laser repetition rate of 10 Hz. Commercially available (001)-oriented MgO was used as a substrate ($10 \times 10 \times 0.5$ mm). Platinum paste was applied between the substrates and heating stage to provide good thermal conductivity. The substrate temperature of 750 °C was measured *via* a pyrometer. N_2 background partial pressure of 8.0×10^{-4} mbar was set *via* a gas inlet line to the vacuum chamber. NH_3 gas was injected through a nozzle near the laser spot at the target. The titanium nitride current collector layer was grown *in situ*, prior to the deposition of the oxynitride film, by conventional PLD using a commercially available TiN target under vacuum with a base pressure of *ca.* 5×10^{-6} mbar. The substrate to target distance, substrate temperature, laser repetition and fluence were the same as above. The TiN and STON layers were both *ca.* 100 nm thick (±5 nm).

Photoelectrochemical characterisation

Photoelectrochemical (PEC) measurements were performed using a three-electrode configuration in the *operando* reactor cell described in Fig. 3. The working and counter electrode were the STON thin films and Pt wire respectively. A KCl saturated Ag/AgCl electrode was used as the reference. An aqueous solution of 0.5 molar NaOH (pH = 13) was used as an electrolyte. For the electrical contact of the STON films a wire was adhered to the TiN current collector to apply the electrical contact to the potentiostat (Metrohm Autolab). The electrically connected area was then insulated with epoxy and the sample then immersed into the electrolyte in the cell. The samples were illuminated with a 405 nm laser diode (Laser2000) which has a 5 mW power output and spot size of *ca.* 0.0308 cm^2. The corresponding light intensity is *ca.* 130 mW cm^{-2}. To measure the dark and light current the laser diode was modulated for 60 second periods (60 seconds on, 60 seconds off). The potentiodynamic measurements were performed at a scan rate of 10 mV s^{-1} under chopped illumination with 4 second periods.

Chemical composition

Rutherford Backscattering (RBS) and Elastic Recoil Detection Analysis (ERDA) were employed to determine the chemical compositions of the STON thin films. RBS provides the metal ratios and oxygen content whereas, ERDA provides nitrogen-to-oxygen ratio. The RBS measurements were performed using a 2 MeV He beam and a silicon PIN diode detector. ERDA was carried out with a 13 MeV ^{127}I beam and the combination of

a time-of-flight spectrometer with a gas ionisation detector. RBS data was analysed using RUMP.[74]

Crystalline properties

XRD measurements were performed using a Seifert X-ray Diffractometer with characteristic Cu Kα radiation 0.154 nm. Theta–2theta scans were performed to determine the out-of-plane orientations of the films.

X-ray photoelectron spectroscopy

The XPS measurements were performed at the SX-ARPES end-station[75] of the Advanced Resonant Spectroscopies (ADRESS) beamline[76] situated at the Swiss Light Source, Paul Scherrer Institute, Switzerland. The photon flux was *ca.* 10^{13} photons per s and focused into a spot size of 30×75 μm^2 on the sample surface at an X-ray grazing incidence angle of 20°. The energy resolution was set to 50 meV and the sample temperature was kept at 298 K. Spectra were calibrated using the C 1s signal due to adventitious carbon situated at 284.8 eV.

X-ray absorption spectroscopy

The time resolved XAS were measured using the quickXAS method[64] at the SuperXAS beamline at the SLS, Paul Scherrer Institut in Switzerland. The polychromatic beam of the 2.9 Tesla superbend was collimated by a Si-coated collimating mirror and subsequently monochromatised by a Si (111) channel-cut crystal of the quickXAS monochromator, which oscillated at 1 Hz frequency with an acquisition time of 500 milliseconds per spectrum. Energy calibration was performed using Pb (L_1 edge $E_0 = 15\ 861$ eV) and Zn (K edge $E_0 = 9659$ eV) thin foils for the Sr K ($E0 = 16\ 105$ eV) and Ta L_3 ($E0 = 9881$ eV) edges, respectively. A focused beam was used with a spot size of 100×100 μm^2. The samples were fixed into the cell and the cell was mounted in grazing incidence to the incoming X-ray beam, with an incident angle between 0–1°. Data analysis was performed using the ProQEXAFS,[77] Athena[78] and Larch[79] software packages.

Author contributions

Conceptualisation, C. L., A. C., O. S., M. N., and D. P.; investigation, C. L., A. C., Z. P., O. S., V. S., M. D.; formal analysis, C. L., A. C., Z. P., V. S.; M. D.; writing – original draft, C. L. and D. P.; writing – review & editing, C. L., A. C., Z. P., O. S., M. N., V. S., M. D., T. S., D. P. and T. L.; funding acquisition, D. P., M. N., T. S., T. L.; supervision, V. S., M. N., D. P., and T. L.

Conflicts of interest

There are no conflicts to declare.

Acknowledgements

The authors would like to thank the Paul Scherrer Institute for financial support through a CROSS grant and the Swiss Light Source for the provision of beamtime at the SuperXAS beamline and to thanks Dr Nick Shepelin for his assistance with the AFM characterisation. TJS thanks Innosuisse and the Swiss Competence Center for Energy Research (SCCER) Heat & Electricity Storage for financial support.

References

1 Y. Tian and C. Y. Zhao, *Appl. Energy*, 2013, **104**, 538–553.
2 B. Parida, S. Iniyan and R. Goic, *Renewable Sustainable Energy Rev.*, 2011, **15**, 1625–1636.
3 J. H. Montoya, L. C. Seitz, P. Chakthranont, A. Vojvodic, T. F. Jaramillo and J. K. Norskov, *Nat. Mater.*, 2016, **16**, 70–81.
4 T. Hisatomi and K. Domen, *Nat. Catal.*, 2019, **2**, 387–399.
5 J. H. Kim, D. Hansora, P. Sharma, J. W. Jang and J. S. Lee, *Chem. Soc. Rev.*, 2019, **48**, 1908–1971.
6 B. A. Pinaud, J. D. Benck, L. C. Seitz, A. J. Forman, Z. Chen, T. G. Deutsch, B. D. James, K. N. Baum, G. N. Baum, S. Ardo, H. Wang, E. Miller and T. F. Jaramillo, *Energy Environ. Sci.*, 2013, **6**, 1983–2002.
7 T. Hisatomi, J. Kubota and K. Domen, *Chem. Soc. Rev.*, 2014, **43**, 7520–7535.
8 T. Takata, C. Pan and K. Domen, *Sci. Technol. Adv. Mater.*, 2015, **16**, 033506.
9 T. Takata and K. Domen, *Dalton Trans.*, 2017, **46**, 10529–10544.
10 J. Seo, Y. Moriya, M. Kodera, T. Hisatomi, T. Minegishi, M. Katayama and K. Domen, *Chem. Mater.*, 2016, **28**, 6869–6876.
11 K. Maeda and K. Domen, *MRS Bull.*, 2011, **36**, 25–31.
12 Y. Zhong, Z. Li, X. Zhao, T. Fang, H. Huang, Q. Qian, X. Chang, P. Wang, S. Yan, Z. Yu and Z. Zou, *Adv. Funct. Mater.*, 2016, **26**, 7156–7163.
13 D. Oka, Y. Hirose, H. Kamisaka, T. Fukumura, K. Sasa, S. Ishii, H. Matsuzaki, Y. Sato, Y. Ikuhara and T. Hasegawa, *Sci. Rep.*, 2014, **4**, 4987.
14 J. Song, T. L. Kim, J. Lee, S. Y. Cho, J. Cha, S. Y. Jeong, H. An, W. S. Kim, Y.-S. Jung, J. Park, G. Y. Jung, D.-Y. Kim, J. Y. Jo, S. D. Bu, H. W. Jang and S. Lee, *Nano Res.*, 2017, **11**, 642–655.
15 Y. Li, J. Li, W. Yang and X. Wang, *Nanoscale Horiz.*, 2020, **5**, 1174–1187.
16 W. Ji, K. Yao, Y.-F. Lim, Y. C. Liang and A. Suwardi, *Appl. Phys. Lett.*, 2013, **103**, 062901.
17 Y. Moriya, T. Takata and K. Domen, *Coord. Chem. Rev.*, 2013, **257**, 1957–1969.
18 R. M. Navarro Yerga, M. C. Alvarez Galvan, F. del Valle, J. A. Villoria de la Mano and J. L. Fierro, *ChemSusChem*, 2009, **2**, 471–485.
19 F. Haydous, M. Döbeli, W. Si, F. Waag, F. Li, E. Pomjakushina, A. Wokaun, B. Gökce, D. Pergolesi and T. Lippert, *ACS Appl. Energy Mater.*, 2019, **2**, 754–763.
20 Y. Wang, S. Wei and X. Xu, *Appl. Catal., B*, 2020, **263**, 118315.
21 K. Kawashima, M. Hojamberdiev, C. Stabler, D. Vrankovic, K. Yubuta, R. Riedel, K. Domen and K. Teshima, *Mater. Renew. Sustain. Energy*, 2017, **6**, 10.
22 M. Pichler, D. Pergolesi, S. Landsmann, V. Chawla, J. Michler, M. Döbeli, A. Wokaun and T. Lippert, *Appl. Surf. Sci.*, 2016, **369**, 67–75.

23 M. Pichler, W. P. Si, F. Haydous, H. Tellez, J. Druce, E. Fabbri, M. El Kazzi, M. Dobeli, S. Ninova, U. Aschauer, A. Wokaun, D. Pergolesi and T. Lippert, *Adv. Funct. Mater.*, 2017, **27**, 1605690.
24 H. Ouhbi and U. Aschauer, *ACS Mater. Lett.*, 2019, **1**, 52–57.
25 J. Druce, H. Téllez, M. Burriel, M. D. Sharp, L. J. Fawcett, S. N. Cook, D. S. McPhail, T. Ishihara, H. H. Brongersma and J. A. Kilner, *Energy Environ. Sci.*, 2014, **7**, 3593–3599.
26 A. Staykov, H. Téllez, T. Akbay, J. Druce, T. Ishihara and J. Kilner, *Chem. Mater.*, 2015, **27**, 8273–8281.
27 A. Staykov, H. Tellez, J. Druce, J. Wu, T. Ishihara and J. Kilner, *Sci. Technol. Adv. Mater.*, 2018, **19**, 221–230.
28 G. M. Rupp, H. Téllez, J. Druce, A. Limbeck, T. Ishihara, J. Kilner and J. Fleig, *J. Mater. Chem. A*, 2015, **3**, 22759–22769.
29 Y. Chen, H. Téllez, M. Burriel, F. Yang, N. Tsvetkov, Z. Cai, D. W. McComb, J. A. Kilner and B. Yildiz, *Chem. Mater.*, 2015, **27**, 5436–5450.
30 Z. Cai, M. Kubicek, J. Fleig and B. Yildiz, *Chem. Mater.*, 2012, **24**, 1116–1127.
31 E. Bucher, W. Sitte, F. Klauser and E. Bertel, *Solid State Ionics*, 2011, **191**, 61–67.
32 F. Wang, T. A. Shifa, X. Zhan, Y. Huang, K. Liu, Z. Cheng, C. Jiang and J. He, *Nanoscale*, 2015, **7**, 19764–19788.
33 H. Wang, K. J. Yakal-Kremski, T. Yeh, G. M. Rupp, A. Limbeck, J. Fleig and S. A. Barnett, *J. Electrochem. Soc.*, 2016, **163**, F581–F585.
34 A. K. Opitz, C. Rameshan, M. Kubicek, G. M. Rupp, A. Nenning, T. Gotsch, R. Blume, M. Havecker, A. Knop-Gericke, G. Rupprechter, B. Klotzer and J. Fleig, *Top. Catal.*, 2018, **61**, 2129–2141.
35 B. Koo, K. Kim, J. K. Kim, H. Kwon, J. W. Han and W. Jung, *Joule*, 2018, **2**, 1476–1499.
36 S. S. Pramana, A. Cavallaro, C. Li, A. D. Handoko, K. W. Chan, R. J. Walker, A. Regoutz, J. S. Herrin, B. S. Yeo, D. J. Payne, J. A. Kilner, M. P. Ryan and S. J. Skinner, *J. Mater. Chem. A*, 2018, **6**, 5335–5345.
37 D. F. Mullica, C. K. Lok, H. O. Perkins and V. V. Young, *Phys. Rev. B: Condens. Matter Mater. Phys.*, 1985, **31**, 4039–4042.
38 A. Robin, *J. Appl. Electrochem.*, 2003, **33**, 37–42.
39 S. J. Yuan, J. J. Chen, Z. Q. Lin, W. W. Li, G. P. Sheng and H. Q. Yu, *Nat. Commun.*, 2013, **4**, 2249.
40 C. Dai, Y. Sun, G. Chen, A. C. Fisher and Z. J. Xu, *Angew. Chem., Int. Ed.*, 2020, **59**, 9418–9422.
41 E. Fabbri, M. Nachtegaal, T. Binninger, X. Cheng, B. J. Kim, J. Durst, F. Bozza, T. Graule, R. Schaublin, L. Wiles, M. Pertoso, N. Danilovic, K. E. Ayers and T. J. Schmidt, *Nat. Mater.*, 2017, **16**, 925–931.
42 H. Kato and A. Kudo, *Phys. Chem. Chem. Phys.*, 2002, **4**, 2833–2838.
43 L. Wei, M. A. S. Adamson and J. Vela, *ChemNanoMat*, 2020, **6**, 1179–1185.
44 V. Rosca, M. Duca, M. T. de Groot and M. T. Koper, *Chem. Rev.*, 2009, **109**, 2209–2244.
45 E. Fabbri, A. Habereder, K. Waltar, R. Kötz and T. J. Schmidt, *Catal. Sci. Technol.*, 2014, **4**, 3800–3821.
46 C. Lawley, M. Nachtegaal, J. Stahn, V. Roddatis, M. Döbeli, T. J. Schmidt, D. Pergolesi and T. Lippert, *Nat. Commun.*, 2020, **11**, 1178.
47 H. Ouhbi and U. Aschauer, *Surf. Sci.*, 2018, **677**, 258–263.
48 M. Pichler, J. Szlachetko, I. E. Castelli, N. Marzari, M. Dobeli, A. Wokaun, D. Pergolesi and T. Lippert, *ChemSusChem*, 2017, **10**, 2099–2106.
49 R. Aguiar, D. Logvinovich, A. Weidenkaff, A. Rachel, A. Reller and S. G. Ebbinghaus, *Dyes Pigm.*, 2008, **76**, 70–75.
50 S.-M. Paek and Y.-I. Kim, *J. Alloys Compd.*, 2014, **587**, 251–254.
51 A. O. Ibidunni, R. L. Masaitis, R. L. Opila, A. J. Davenport, H. S. Isaacs and J. A. Taylor, *Surf. Interface Anal.*, 1993, **20**, 559–564.
52 T. S. Wu, Y. C. Chen, Y. F. Shiu, H. J. Peng, S. L. Chang, H. Y. Lee, P. P. Chu, C. W. Hsu, L. J. Chou, C. W. Pao, J. F. Lee, J. Kwo, M. Hong and Y. L. Soo, *Appl. Phys. Lett.*, 2012, **101**, 022408.
53 X. Cheng, B. J. Kim, E. Fabbri and T. J. Schmidt, *ACS Appl. Mater. Interfaces*, 2019, **11**, 34787–34795.
54 A. Mahmood, S. Azam, M. Irfan, M. A. Kamran, T. Alharbi, A. Majid, M. W. Iqbal, S. Muhammad, A. G. Al-Sehemi, S. A. Khan and S. Goumri-Said, *Mater. Sci. Semicond. Process.*, 2020, **107**, 104800.
55 R. B. Greegor, N. E. Pingitore Jr and F. W. Lytle, *Science*, 1997, **275**, 1452–1454.
56 F. Farges, *J. Non-Cryst. Solids*, 1996, **204**, 53–64.
57 A. Staykov, S. Fukumori, K. Yoshizawa, K. Sato, T. Ishihara and J. Kilner, *J. Mater. Chem. A*, 2018, **6**, 22662–22672.
58 J. Lee, W. D. Lu and E. Kioupakis, *Nanoscale*, 2017, **9**, 1120–1127.
59 X. Wen, Y. Feng, S. Huang, F. Huang, Y.-B. Cheng, M. Green and A. Ho-Baillie, *J. Mater. Chem. C*, 2016, **4**, 793–800.
60 H. Abe, G. Aquilanti, R. Boada, B. Bunker, P. Glatzel, M. Nachtegaal and S. Pascarelli, *J. Synchrotron Radiat.*, 2018, **25**, 972–980.
61 D. Ferri, M. A. Newton and M. Nachtegaal, *Top. Catal.*, 2011, **54**, 1070–1078.
62 G. L. Chiarello and D. Ferri, *Phys. Chem. Chem. Phys.*, 2015, **17**, 10579–10591.
63 C. F. J. König, J. A. van Bokhoven, T. J. Schildhauer and M. Nachtegaal, *J. Phys. Chem. C*, 2012, **116**, 19857–19866.
64 M. Nachtegaal, O. Müller, C. König and R. Frahm, in *X-Ray Absorption and X-Ray Emission Spectroscopy*, ed. J. A. V. Bokhoven and C. Lamberti, John Wiley & Sons, 2016, ch. 7, pp. 155–183, DOI: 10.1002/9781118844243.ch7.
65 D. Baurecht and U. P. Fringeli, *Rev. Sci. Instrum.*, 2001, **72**, 3782–3792.
66 A. Urakawa, T. Bürgi and A. Baiker, *Chem. Eng. Sci.*, 2008, **63**, 4902–4909.
67 H. Yoshida, S. Nonoyama and Y. Y. T. Hattori, *Phys. Scr.*, 2005, **115**, 813–815.
68 P. Zhang, J. Zhang and J. Gong, *Chem. Soc. Rev.*, 2014, **43**, 4395–4422.
69 X. Deng and H. Tüysüz, *ACS Catal.*, 2014, **4**, 3701–3714.

70 K. J. May, C. E. Carlton, K. A. Stoerzinger, M. Risch, J. Suntivich, Y.-L. Lee, A. Grimaud and Y. Shao-Horn, *J. Phys. Chem. Lett.*, 2012, **3**, 3264–3270.
71 T. Das, J. D. Nicholas and Y. Qi, *J. Mater. Chem. A*, 2017, **5**, 25031–25043.
72 E. Fabbri and T. J. Schmidt, *ACS Catal.*, 2018, **8**, 9765–9774.
73 X. Sun, F. Wu, G. Liu and X. Xu, *J. Mater. Chem. A*, 2018, **6**, 20760–20768.
74 L. R. Doolittle, *Nucl. Instrum. Methods Phys. Res., Sect. B*, 1986, **15**, 227–231.
75 V. N. Strocov, X. Wang, M. Shi, M. Kobayashi, J. Krempasky, C. Hess, T. Schmitt and L. Patthey, *J. Synchrotron Radiat.*, 2014, **21**, 32–44.
76 V. N. Strocov, T. Schmitt, U. Flechsig, T. Schmidt, A. Imhof, Q. Chen, J. Raabe, R. Betemps, D. Zimoch, J. Krempasky, X. Wang, M. Grioni, A. Piazzalunga and L. Patthey, *J. Synchrotron Radiat.*, 2010, **17**, 631–643.
77 A. H. Clark, J. Imbao, R. Frahm and M. Nachtegaal, *J. Synchrotron Radiat.*, 2020, **27**, 551–557.
78 B. Ravel and M. Newville, *J. Synchrotron Radiat.*, 2005, **12**, 537–541.
79 M. Newville, *J. Phys.: Conf. Ser.*, 2013, **430**, 012007.